

DES J0454–4448: discovery of the first luminous $z \geq 6$ quasar from the Dark Energy Survey

S. L. Reed,^{1,2*} R. G. McMahon,^{1,2} M. Banerji,^{1,2,3} G. D. Becker,^{1,2,4}
E. Gonzalez-Solares,¹ P. Martini,^{5,6} F. Ostrovski,^{1,2} M. Rauch,⁷ T. Abbott,⁸
F. B. Abdalla,³ S. Allam,^{4,9} A. Benoit-Levy,³ E. Bertin,¹⁰ E. Buckley-Geer,⁹
D. Burke,¹¹ A. Carnero Rosell,¹² L. N. da Costa,^{12,13} C. D’Andrea,¹⁴ D. L. DePoy,¹⁵
S. Desai,¹⁶ H. T. Diehl,⁹ P. Doel,³ C. E. Cunha,¹⁷ J. Estrada,⁹ A. E. Evrard,¹⁸
A. Fausti Neto,¹³ D. A. Finley,⁹ P. Fosalba,¹⁹ J. Frieman,⁹ D. Gruen,^{16,20}
K. Honscheid,⁵ D. James,⁸ S. Kent,⁹ K. Kuehn,²¹ N. Kuropatkin,⁹ O. Lahav,³
M. A. G. Maia,^{12,13} M. Makler,²² J. Marshall,¹⁵ K. Merritt,⁹ R. Miquel,²³ J. Mohr,¹⁶
B. Nord,⁹ R. Ogando,¹² A. Plazas,²⁴ K. Romer,¹⁴ A. Roodman,^{11,17} E. Rykoff,¹¹
M. Sako,²⁵ E. Sanchez,²⁶ B. Santiago,²⁷ M. Schubnell,¹⁸ I. Sevilla,²⁶ C. Smith,⁸
M. Soares-Santos,⁹ E. Suchyta,^{5,28} M. E. C. Swanson,^{5,28,29} G. Tarle,¹⁸ D. Thomas,^{14,30}
D. Tucker,⁹ A. Walker⁸ and R. H. Wechsler^{17,31}

Affiliations are listed at the end of the paper

Accepted 2015 September 1. Received 2015 August 27; in original form 2015 April 13

ABSTRACT

We present the first results of a survey for high-redshift, $z \geq 6$, quasars using iZY multicolour photometric observations from the Dark Energy Survey (DES). Here we report the discovery and spectroscopic confirmation of the $z_{AB}, Y_{AB} = 20.2, 20.2$ ($M_{1450} = -26.5$) quasar DES J0454–4448 with a redshift of $z = 6.09 \pm 0.02$ based on the onset of the Ly α forest and an H I near zone size of $4.1^{+1.1}_{-1.2}$ proper Mpc. The quasar was selected as an i -band drop out with $i-z = 2.46$ and $z_{AB} < 21.5$ from an area of $\sim 300 \text{ deg}^2$. It is the brightest of our 43 candidates and was identified for spectroscopic follow-up solely based on the DES $i-z$ and $z-Y$ colours. The quasar is detected by *WISE* and has $W1_{AB} = 19.68$. The discovery of one spectroscopically confirmed quasar with $5.7 < z < 6.5$ and $z_{AB} \leq 20.2$ is consistent with recent determinations of the luminosity function at $z \sim 6$. DES when completed will have imaged $\sim 5000 \text{ deg}^2$ to $Y_{AB} = 23.0$ (5σ point source) and we expect to discover 50–100 new quasars with $z > 6$ including 3–10 with $z > 7$ dramatically increasing the numbers of quasars currently known that are suitable for detailed studies.

Key words: galaxies: active – galaxies: formation – galaxies: high-redshift – quasars: individual: DES J0454-4448 – dark ages, reionization, first stars.

1 INTRODUCTION

High-redshift quasars act as important probes of the very early Universe. They can be used to study the formation and evolution of the first supermassive black holes and to provide insight into the properties of the inter-galactic medium (IGM). The Ly α forest and

associated absorption lines bluewards of the Ly α peak in a high-redshift quasar spectrum give a direct measurement of the neutral hydrogen in the IGM (Fan et al. 2006). Detailed studies of the ionized near zone in quasars can be used to investigate the ionization state and evolution of the neutral hydrogen fraction at $z > 6$ (Bolton & Haehnelt 2007). Cosmologically distributed intervening quasar absorption lines allow us to map the distribution of gas in the IGM as well as the metal content. Identifying larger numbers of high-redshift quasars would enable such studies to be conducted further

* E-mail: sr525@ast.cam.ac.uk

back in cosmic time along independent lines of sight through the IGM.

Spectra of quasars from $z \sim 2$ (Gunn & Peterson 1965) up to $z \sim 6$ (Fan et al. 2006; Becker, Rauch & Sargent 2007) indicate that the IGM is highly ionized ($n_{\text{H I}}/n_{\text{H}} \leq 10^{-4}$) and therefore that reionization was complete at earlier epochs. The 2σ lower-bound for the Epoch of Reionization is estimated to be at $z \sim 6$ from cosmic microwave background (CMB) measurements (Planck Collaboration XIII 2015). The discovery of a large sample of new high-redshift quasars at $z > 6$ would allow this important epoch to be studied in detail. Even the discovery of a few new objects can be valuable if they have extreme properties, such as being very bright (Wu et al. 2015) or very distant (Mortlock et al. 2011).

Previous surveys for high-redshift ($z \geq 6.0$) quasars (e.g. Fan et al. 2006; Jiang et al. 2009; Willott et al. 2010; Mortlock et al. 2012; Venemans et al. 2013, 2015; Carnall et al. 2015) have already led to the discovery of ~ 50 quasars at $z \geq 6.0$. Most of these surveys have employed purely optical photometric data sets such as those provided by the Sloan Digital Sky Survey (SDSS) and the Canada–France–Hawaii Telescope Survey (CFHTLS). The new optical photometry provided by the Dark Energy Survey (DES; The Dark Energy Survey Collaboration 2005) provides one notable advantage over most of these previous optical surveys from the point of view of high-redshift quasar selection. The Dark Energy Camera (DECam) CCD detectors are optimized to extend to the near-infrared (NIR) wavelengths of $\sim 1 \mu\text{m}$. The associated *grizY* filter-set therefore allows detection of quasars out to higher redshifts than was possible with previous optical surveys. The DES z -band and the redder Y -band coupled with the large area of the celestial sky not previously surveyed and the increased depth over previous surveys enables detection of Ly α at $6.5 \lesssim z \lesssim 7.2$. In previous optical surveys the sensitivity in the z -band resulted in making it increasingly difficult to find quasars with increasing redshift.

Here, we present the first search for high-redshift quasars in the DES Science Verification Data. DES magnitudes, NIR VISTA magnitudes and *Wide Infrared Survey Explorer* (WISE) magnitudes are quoted on the AB system. The conversions from Vega to AB that have been used for the VISTA data are: $J_{\text{AB}} = J_{\text{Vega}} + 0.937$ and $K_{\text{SAB}} = K_{\text{Vega}} + 1.839$, these are taken from the Cambridge Astronomical Survey Unit’s website.¹ The conversions for the ALLWISE data are $W1_{\text{AB}} = W1_{\text{Vega}+2.699}$ and $W2_{\text{AB}} = W2_{\text{Vega}+3.339}$ which are given in Jarrett et al. (2011) and in the ALLWISE explanatory supplement.² When required a flat cosmology with $\Omega_{\text{m}0} = 0.3$ and $H_0 = 70.0$ was used.

2 DES DATA

The DES is a 5000 deg² optical survey in the southern celestial hemisphere being conducted using the Dark Energy Camera (DECam; Flaugher et al. 2012). DECam is mounted on the Blanco 4-metre telescope at the Cerro Tololo Inter-American Observatory (CTIO) and the data are processed by the DES data management system (Desai et al. 2012; Mohr et al. 2012). The 570-megapixel DECam has a field of view of 3 deg² with 0.27 arcsec per pixel. To allow for a good detection efficiency of high-redshift objects,

¹ <http://casu.ast.cam.ac.uk/surveys-projects/vista/technical/filter-set>

² The ALLWISE explanatory supplement, http://wise2.ipac.caltech.edu/docs/release/allwise/expsup/sec5_3e.html, directs the reader to the WISE All-Sky explanatory supplement for the conversions; http://wise2.ipac.caltech.edu/docs/release/allsky/expsup/sec4_4h.html#summary.

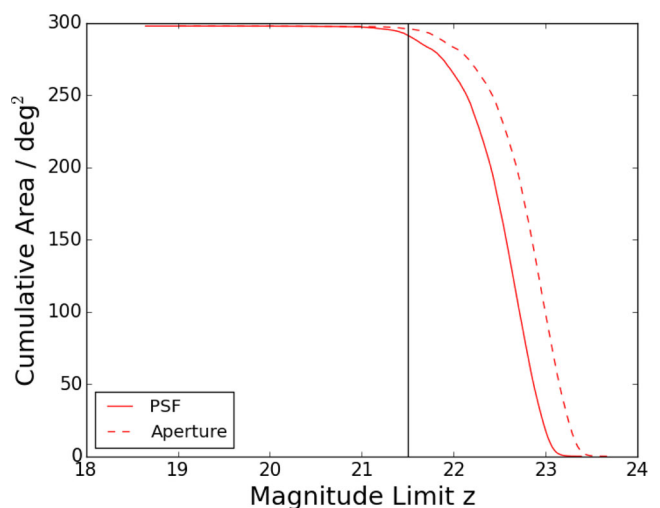


Figure 1. Cumulative area versus 10σ z -band depth in a 2 arcsec diameter aperture and PSF magnitudes for the DES SVA1 data. The aperture magnitudes were converted to PSF magnitudes using the median offset between PSF magnitude and aperture magnitude for point sources from the whole SVA1 data set. Our magnitude limit of $z_{\text{psf}} < 21.5$ is shown as the vertical line. The aperture magnitude limits were taken from the DES mangle (Swanson et al. 2008) products.

DECam CCDs are very sensitive to the red part of the spectrum. These fully depleted, 250- μm thick detectors have been developed at the Lawrence Berkeley National Laboratory to be used for DES. The quantum efficiency of these devices in the z -band is above 50 per cent, almost an order of magnitude higher than traditional thinned devices. This also allows the Y -band observations to be taken within the same survey reducing the need for follow-up photometry to confirm high-redshift quasar candidates. The combination of depth, red sensitivity and area provided by DES, makes it an ideal experiment for searching for luminous quasars at high redshift in the southern celestial hemisphere.

The DES survey area also overlaps the near-infrared VISTA Hemisphere Survey (VHS; McMahon et al. 2013) at $\sim 1 - 2 \mu\text{m}$ and the all-sky WISE data at 3.4, 4.6, 12 and 22 μm . These two surveys therefore provide infrared photometry for high-redshift quasar candidates selected in DES (Banerji et al. 2015).

The DECam obtained its first light images in 2012 September and this was followed by a period of Commissioning and Science Verification observations (SV hereafter) lasting between 2012 October and 2013 February. In this work, we utilize the Science Verification First Annual Data Release (SVA1) by DES Data Management to conduct our high-redshift quasar search. The SVA1 observations were designed to reach the full DES survey depth expected after the nominal five-year survey period. However, the depth across the SVA1 area is non-uniform. Fig. 1 shows the cumulative area in the DES SVA1 region down to a given 10σ depth in the z -band derived from mangle (Swanson et al. 2008) based polygon depth maps. These 10σ depth maps are calculated for a 2 arcsec diameter apertures. These values will depend on the seeing in each polygon and have been converted to PSF magnitudes using the median difference for all stellar objects (as defined in section III) The median of these differences ($z_{\text{psf}} - z_{2\text{arcsec}}$) was found to be -0.28 with a $\sigma_{\text{MAD}} = 0.066$. This offset was applied to the magnitude limit calculated as shown in Fig. 1. In this paper, PSF and model magnitudes are used. The PSF magnitude is the PSF magnitude and the model magnitude is the magnitude once a galaxy model has been fitted to pick up the

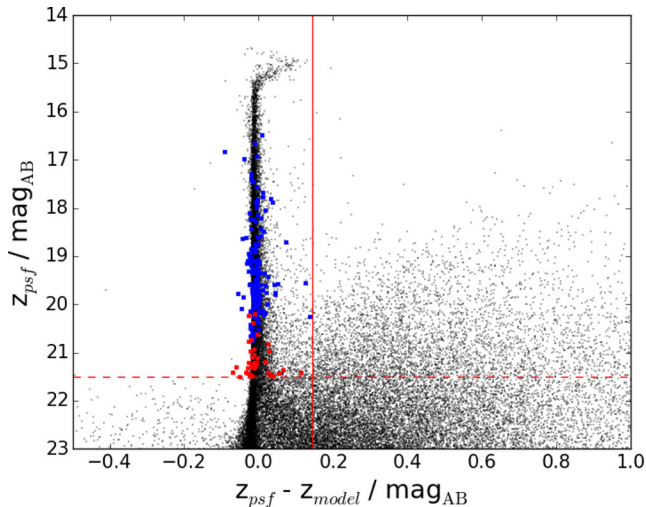


Figure 2. The black points are all the objects on one tile from the survey and the red points show the quasar candidates after the final stage of the selection in Section 3. A clear locus can be seen at 0.0 on the horizontal axis. The blue points are known quasars taken from the catalogue given in Véron-Cetty & Véron (2010) with $z > 2.0$. Below this redshift host galaxy contamination can occur. The median of the Véron 2010 sample is 0.015 and the $\sigma_{\text{MAD}} = 0.052$. The solid vertical line shows the cut used to select point sources. The dashed horizontal line shows the magnitude limit used.

flux in the extended wings of the object. Both of these parameters are produced by the DES data management pipeline. As detailed later, a flux-limited sample down to a depth of $z_{\text{psf}} < 21.5$ is used for the high-redshift quasar search presented here, which corresponds to a total survey area of 291 deg².

3 QUASAR CANDIDATE SELECTION

Whilst low-redshift ($z \lesssim 2$) quasars have characteristically blue optical colours (from ultraviolet excess; Schmidt & Green 1983) at $z \gtrsim 4$ quasars start to become red in the shorter wavelength optical bands (Hook & McMahon 1998; Storrie-Lombardi et al. 2001). The observer frame optical colours of these high-redshift quasars are characterized by absorption due to neutral hydrogen in the intergalactic medium in the rest-frame UV shortwards of the Lyman α ($\lambda_{\text{rest}} = 1216 \text{ \AA}$) emission line. At $z = 6$ the Ly α line is redshifted to 8512 \AA which leads to red ($i - z$) colours for quasars at these redshifts. These high-redshift quasars are therefore selected in optical surveys as i -band drop outs (Fan et al. 2000). Below we detail our selection method for isolating high-redshift quasar candidates from the DES imaging data. PSF magnitudes are used throughout (unless otherwise stated) as they provide the best measure of flux for unresolved point-like sources.

The primary colour selection used is an ($i - z$) colour criterion, which is based on the selection used by Fan et al. (2001). The Fan et al. (2001) SDSS selection of ($i - z$) > 2.2 was mapped on to the DES filter system as follows. First we selected point-like objects in the area of overlap between the DES and SDSS surveys, as those having $z_{\text{psf}} - z_{\text{model}} < 0.145$. This point source selection is illustrated in Fig. 2 and is detailed below. The DES and SDSS sources were matched using a radius of 2.16 arcsec (0:006). A least-squares linear fit was carried out on a running median of the colours. A window size of 50 was used for the median and the data was sorted by ($i - z$)_{SDSS} and then sparsely sampled along

Table 1. Summary of the steps in the high-redshift quasar selection process.

Step	Description	Number removed	Number remaining
	Number of objects in data base		40 129 963
1	Flag criteria	3 170 496	36 959 467
2	$z_{\text{psf}} \leq 21.5$ and $\sigma_z < 0.1$	29 760 121	7 199 346
3	$z_{\text{psf}} - z_{\text{model}} < 0.145$	2 409 240	4 790 106
4	$i_{\text{psf}} - z_{\text{psf}} > 1.694$	4 766 589	23 517
5	g_{psf} and $r_{\text{psf}} > 23.0$	12 985	10 532
6	σ_g and $\sigma_r > 0.1$	371	10 161
7	$z_{\text{psf}} - Y_{\text{psf}} < 0.5$	92	10 069
8a	Y_{psf} not equal to 99	8725	1344
8b	$Y_{\text{psf}} < 23.0$	506	838
9	Forced photometry in the r band	372	466
10	Cosmic ray removal	489	77
11	Visual inspection	34	43
12	$\phi_{i,z} > 4$	39	4

the ($i - z$)_{SDSS} direction with a stride of 10 to determine the colour term between the two surveys:

$$(i - z)_{\text{DES}} = 0.72(i - z)_{\text{SDSS}} + 0.111 \quad (1)$$

Based on this and the Fan et al. (2001) selection criterion we derive an equivalent colour criterion of ($i - z$)_{DES} > 1.694 .

We now list each of the steps in our high-redshift quasar selection process, which are also summarized in Table 1.

(i) High-redshift quasar and other rare object searches are often contaminated by a large number of artefacts. These spurious sources often dominate outlier regions of colour space that are also populated by smaller numbers of real objects. In fact it is safe to assume that most outliers in an unfiltered catalogue are junk. The first step therefore involved artefact removal at the catalogue level. Objects that were flagged by the DES data management SVA1 pipeline as having bright neighbours that were close enough to bias photometry, being originally blended with another object or having at least one saturated pixel were provisionally labelled as junk. If they were also flagged as having at least one low-weight pixel in the measurement image within the isophotal footprint or in the filtered detection image then this was confirmed and they were removed. A combination of the weight flags and the image flags was used to ensure that faint objects undetected in some of the bands were retained while removing bright saturated objects and bleed trails. The flags cut resulted in 36 959 467 objects remaining of the original 40 129 963 in the DES SVA1 release. Examples of the artefacts removed in this step are shown in Appendix A1.

(ii) A flux limited sample was then created by limiting the sample to sources with

$$z_{\text{psf}} \leq 21.5 \text{ and } \sigma_z < 0.1 \quad (2)$$

(iii) Objects were required to satisfy a point source criteria of

$$z_{\text{psf}} - z_{\text{model}} < 0.145 \quad (3)$$

which is the star-galaxy classifier defined in the SDSS photometric survey (Stoughton et al. 2002) and SDSS quasar selection (Richards et al. 2002). After this step there were 4 790 106 objects remaining. This star-galaxy separation criterion is shown in Fig. 2. The stellar locus is clearly situated at $z_{\text{psf}} - z_{\text{model}} \sim 0$. We can see that the star-galaxy separation starts to become less reliable at fainter magnitudes but the stellar locus is still clearly visible down to $z < 21.5$, which is the flux limit imposed on our sample.

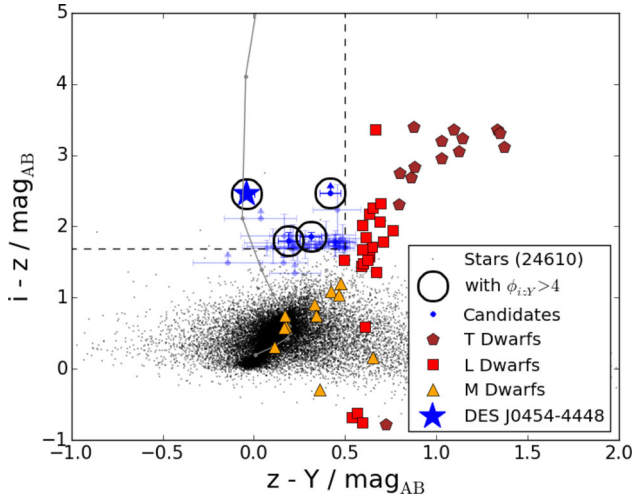


Figure 3. The black points represent all objects that have $z_{\text{psf}} - z_{\text{model}} < 0.145$ and are detected in the i , z and Y bands from one tile of the survey. The blue points are the candidate objects that satisfy the first 11 steps of the selection criteria. The objects that pass the final step are circled while the others are faded. The blue star shows the location of the confirmed quasar. The grey line shows a simulated quasar track starting from $z = 5$ and incrementing by 0.1 to $z = 6.4$. Objects that have $i = 99$ (are undetected in the i band) pass the selection criteria and are here plotted with arrows to indicate that they are lower limits in $i - z$. The objects outside the selection box are limits in the i band where the survey is particularly shallow. Many of the objects are situated at the lower right of the selection box which suggests that they are cool stars scattered in by random photometric errors. This is supported by the large errors that many of them have which overlap the selection box edges. The red, orange and brown points are known brown dwarfs found with UKIDSS and converted using the spectra and the DES band passes.

(iv) The colour criterion derived above:

$$(i - z)_{\text{DES}} > 1.694 \quad (4)$$

was then applied leaving 23 517 objects.

(v) As high-redshift ($z \gtrsim 6$) quasars should not have detectable flux in their rest-frame shortwards of the hydrogen limit at $\lambda_{\text{rest}} = 912 \text{ \AA}$ corresponding to $\lambda_{\text{obs}} \sim 6500 \text{ \AA}$ they should be undetected in the g or r bands. Visual inspection of a sample of candidates indicated that some had significant detectable flux in g and r . We therefore applied the following criterion to the g - and r -band measurements:

$$g_{\text{psf}} > 23.0 \text{ and } r_{\text{psf}} > 23.0 \quad (5)$$

which were chosen as this ruled out almost all of the objects that were reliably detected without removing undetected sources in regions of particularly deep photometry.

(vi) There were a few objects that were very faint in the g or r band but were in a very deep part of the survey and still had a reliable detection in these bluer bands. To remove these detected objects an error threshold of σ_g and $\sigma_r > 0.1$ was used i.e. objects with σ_g and $\sigma_r \sim 0.2$ (5σ detections) are retained since there is a finite probability that they have zero flux.

(vii) Cool dwarf stars, such as L and T-dwarfs, in our own Milky Way, are the main astrophysical contaminants in high-redshift quasar searches. These were removed using a colour cut of

$$z_{\text{psf}} - Y_{\text{psf}} < 0.5 \quad (6)$$

The colour selection can be seen in Fig. 3 which shows the cool dwarf locus clearly distinct from the selection box in terms of the

$z - Y$ colour. We note that a blue $z - Y$ cut will also potentially remove higher redshift quasars at $z \gtrsim 6.5$, at which point the Ly α peak begins to move into the DES Y band, making the $z - Y$ colour redder. In the future, we will use NIR data, particularly in the J band from VHS, to push our quasar search to higher redshifts. This selection will cover $z - Y$ dropouts, rather than $i - z$, and will be discussed further in future work.

(viii) At this stage many of the objects left were bright artefacts in the z band which were not present in any of the other bands. To limit the numbers of these that was present in the sample two Y -band magnitude cuts were used. First objects with bad Y -band photometry ($Y_{\text{psf}} = 99$) were removed and then those with $Y_{\text{psf}} < 23.0$. These cuts ensured that objects were detected in the Y band as well reducing their likelihood of being a z -band artefact.

(ix) Following these cuts, many of the objects that remained had PSF magnitudes of 99 in the r band. They corresponded to two classes of objects: either very bright objects or those at the r -band detection limit. The bright objects were removed using list driven forced photometry in the r band. For each object we identified the brightest pixel in a box of 3×3 pixels centred on the position of the object and required that it was no more than 10 analogue to digital units greater than the median value in a 30 arcsec box around the object. This corresponds roughly to three times the median σ_{MAD} (3.06) above the median of the median values (0.147) of the images in the data release. A conservative threshold of 10 was used to filter these bright objects to ensure that any faint objects which may correspond to high-redshift quasars, were not removed.

(x) Most of the objects that remained at this stage were cosmic ray detections in the z band. These were removed based on the differences between adjacent pixels (as a proxy for the local pixel gradients) as a cosmic ray would be more abrupt in terms of its pixel gradient than a real object. In future DES data releases, a new method of cosmic ray reduction will be included in the pipeline processing.

(xi) Following these steps there were few enough candidates to cut down by systematic visual inspection. The visual inspection stage removed 34 spurious sources such as cosmic rays, satellite trails and diffraction spikes. At the end of this stage we have 43 candidate high-redshift quasars.

(xii) We ranked these 43 final candidates based on an error weighted photometric selection metric for follow-up spectroscopy. The selection metrics ϕ_{iz} and ϕ_{zY} combine to give ϕ_{izY} which essentially constitutes an error-weighted measure of how far into the colour-selection box, shown in Fig. 3, each candidate lies.

$$\phi_{iz} = \frac{(i_{\text{psf}} - z_{\text{psf}}) - 1.694}{\sqrt{i_{\text{err}}^2 + z_{\text{err}}^2}} \quad (7)$$

$$\phi_{zY} = \frac{0.5 - (z_{\text{psf}} - Y_{\text{psf}})}{\sqrt{z_{\text{err}}^2 + Y_{\text{err}}^2}} \quad (8)$$

$$\phi_{izY} = \sqrt{\frac{\phi_{iz}^2}{|\phi_{iz}|} + \frac{\phi_{zY}^2}{|\phi_{zY}|}} \quad (9)$$

For those sources undetected in the i band, the i -band magnitude limit at the source position was used instead in the computation of ϕ_{iz} and the error set to 0.2.

This selection led to prioritising four of the 43 candidates as highly viable high-redshift quasar candidates with $\phi_{izY} > 4$ from the 291 deg^2 region. The distribution of ϕ values can be seen in Fig. 4 where the four candidates have been circled. One of these candidates clearly has much larger values of ϕ than the other three and this

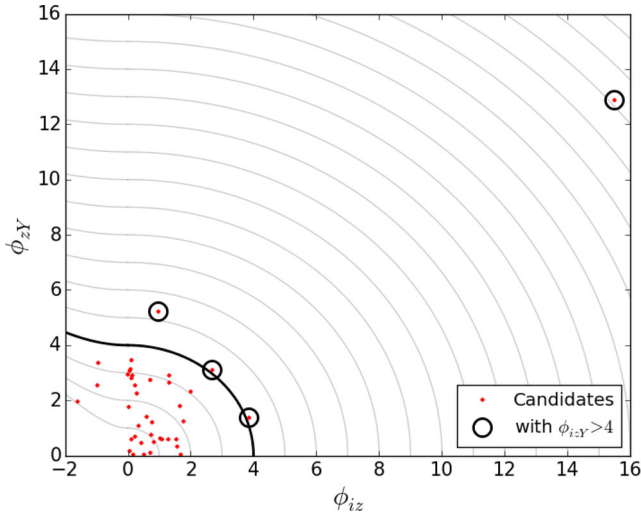


Figure 4. The ϕ_{izY} selection metric. Here the x -axis is the ϕ_{iz} defined in equation (7) and the y -axis is ϕ_{zY} . The four objects with $\phi_{izY} > 4$ are circled and the object that was confirmed as a quasar has the highest value of both Φ_{iz} and Φ_{zY} the figure.

object (DES J0454–4448) with $z_{AB} = 20.2$ was therefore selected for follow-up spectroscopy as our most promising first high-redshift quasar candidate from the DES data. DES J0454–4448 is shown across the DES and VISTA bands in Fig. 5. In these cutout images the absence of flux in the g and r bands can be clearly seen along with the increase in brightness from the i to z bands.

4 DES J0454–4448

The photometric data for DES J0454–4448 is summarized in Table 2. This includes the DES photometry (g , r , i , z and Y) as well as infrared magnitudes from the VISTA Hemisphere Survey (J and K) and the *AllWISE* data release of the *WISE* All-Sky Survey (Wright et al. 2010; $W1$ and $W2$). Blain et al. (2013) have studied the infrared *WISE* colours of known high-redshift quasars finding that they are typically bluer than the $W1_{AB} - W2_{AB} > 0.16$ selection cut used to select lower redshift AGN such as in Stern et al. (2012). The colour ($W1_{AB} - W2_{AB} = 0.05$) of this object supports this and agrees with the locus of known high-redshift quasars matched to the *WISE* data. The colour also agrees with the predicted track in Assef et al. (2010) as shown in Fig. 6. As the resolution of *WISE* (6.1 arcsec and 6.4 arcsec in $W1$ and $W2$, respectively) is quite large compared to the separation of the object and its nearest neighbour (4.89 arcsec) it is debatable if the magnitude corresponds solely to the quasar.

Spectroscopic follow-up of DESJ0454–4448 was conducted using the Magellan Echelle (MagE) spectrograph (Marshall et al. 2008) on the 6.5 m Clay telescope at the Las Campanas Observa-

Table 2. Properties of DES J0454–4448. The g -band magnitude is given as a 10σ magnitude limit for a 2 arcsec aperture.

DES J0454–4448	
DES tilename	DES0453–4457
RA (J2000)	73.507 45 ($04^{\text{h}}54^{\text{m}}01^{\text{s}}.79$)
Dec. (J2000)	$-44.808\ 64$ ($-44^{\circ}48'31''.1$)
Redshift	6.09 ± 0.02
g	> 23.41
r	25.30 ± 0.25 [AB]
i	22.66 ± 0.05 [AB]
z	20.20 ± 0.01 [AB]
Y	20.24 ± 0.04 [AB]
J	20.24 ± 0.07 [AB]
Ks	20.12 ± 0.17 [AB]
$W1$	19.68 ± 0.08 [AB]
$W2$	19.62 ± 0.14 [AB]
M_{1450}	-26.48 ± 0.03
R_{NZ}	$4.1^{+1.1}_{-1.2}$ Mpc
$R_{NZ, corrected}$	$4.8^{+1.3}_{-1.4}$ Mpc

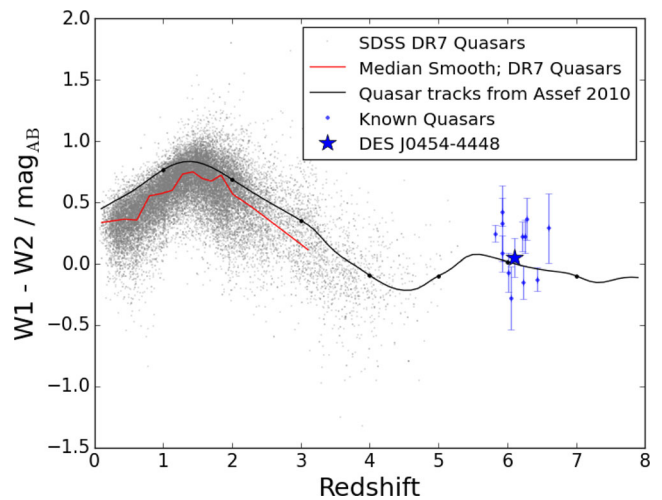


Figure 6. The figure shows the evolution in $W1 - W2$ colour with redshift of known quasars. The grey points are known low-redshift quasars from SDSS DR7 with the red line being a median smooth of these data. This allows comparison with the predicted track from Assef et al. (2010), which is shown by the black line. The blue points are a subsample of the known high-redshift quasars matched to *WISE*, these objects were matched to the *ALLWISE* data and then visually inspected to remove blended sources in *WISE*. The large blue star is DES J0454–4448.

tory in Chile. Two 10 min exposures were taken on the night of 2013 December 2 in variable conditions. The data were reduced and the one-dimensional spectrum combined using a custom set of

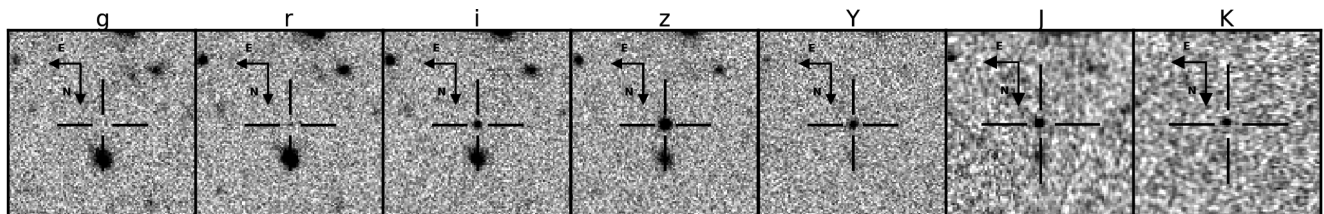


Figure 5. Cutouts of our spectroscopically confirmed quasar, DESJ0454–4448 in each of the DES (g , r , i , z and Y) and VHS (J and K) wavebands. The boxes are 30 arcsec across and the quasar is the central object.

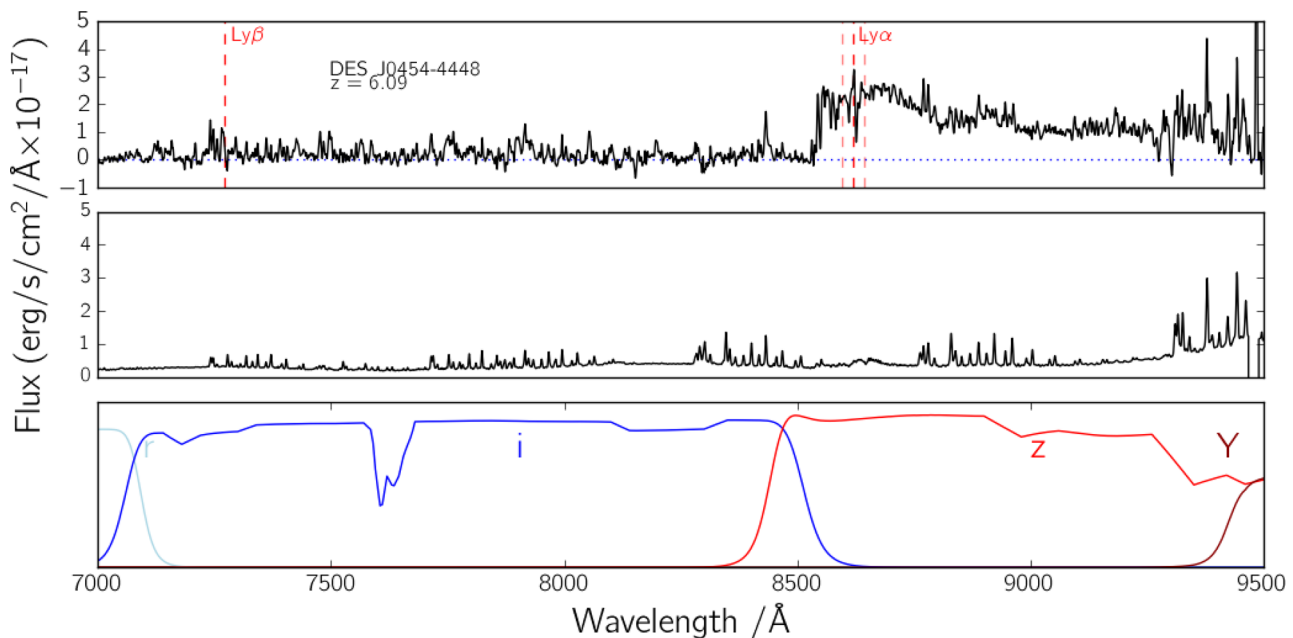


Figure 7. The discovery spectrum of DES J0454–4448 at $z = 6.09$. It shows the characteristic flux deficit bluewards of Ly α indicative of a high-redshift quasar. The red vertical lines over the spectrum show the positions of the Ly β and the Ly α emission line redshifted to $z = 6.09$ as well as the errors on the position of Ly α from the error in the redshift. The middle plot shows the error spectra and the bottom plot indicates the efficiencies of the DES filters as a function of wavelength. Both the object spectra and associated error spectra have been smoothed to the same degree using a Gaussian filter.

IDL routines. The discovery spectrum for the quasar can be seen in Fig. 7.

Measuring the quasar redshift from emission lines in the present spectrum is difficult due to the strong attenuation of Ly α ($\lambda_{\text{rest}} = 1215.67 \text{ \AA}$) and the modest quality and limited wavelength range of the data which does not cover the wavelength range to detect CIV(1549) or SiIV+OIV](1400) which at $z \geq 6.00$ have observed wavelength that $\lambda \geq 9800 \text{ \AA}$. We therefore rely on the apparent onset of Ly α forest absorption to estimate the redshift. This approach has been previously used for weak lined quasars such as BL Lac objects (Danforth et al. 2010).

A series of absorption lines appears over $8530 \lesssim \lambda \lesssim 8630 \text{ \AA}$, which we interpret as the expected Ly α absorption in the quasar’s near zone. The reddest of these lines falls at 8626 \AA , which corresponds to a Ly α redshift of $z = 6.096$. We tentatively detect the quasar’s Si II 1260 \AA emission line with a peak wavelength near 8920 \AA , though it is contaminated by skyline subtraction residuals, corresponding to a redshift of 6.077. Combining these estimates gives a mean redshift and standard deviation: $z = 6.09 \pm 0.01$. To reflect the systematic uncertainty in the redshift we follow Fan et al. (2006) and adopt an total uncertainty of 0.02 to take account of the observed offsets in redshifts between low- and high-ionization lines in quasars.

The quasar continuum is strongly attenuated at $\lambda \leq 8530 \text{ \AA}$. Following the method outlined in Fan et al. (2006), we take the edge of the proximity zone to be the point where the ratio between the continuum flux and the spectrum first falls below 0.1 bluewards of the Ly α peak. Here the intrinsic continuum is roughly estimated using a composite from low-redshift SDSS spectrum (as used in Mortlock et al. 2011) normalized to the flux between 1268 and 1295 \AA . The near-zone size for an edge at 8530 \AA and the quasar redshift estimated above is $4.1^{+1.1}_{-1.2}$ proper Mpc, the error in this measurement is dominated by the error in the redshift. In Fig. 8 the normalized flux and the extent of the near zone are shown. The

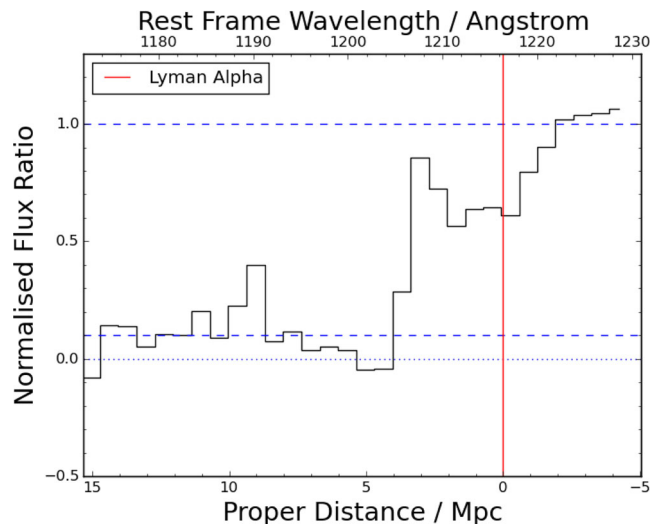


Figure 8. In this plot the ratio of the continuum flux and the spectrum is shown. The red vertical line shows the position of the Lyman α peak. The dashed blue line is at a flux ratio of 0.1 and the dotted blue line show the zero level. The near zone has a size of $4.1^{+1.1}_{-1.2}$ proper Mpc.

corrected near-zone size of this object is found to be consistent with the measured relationship in the Carilli et al. (2010) study. Due to the low signal to noise of the data, no constraints can be put on the optical depth at this redshift.

5 DISCUSSION

The number density estimates based on the Willott et al. (2010) luminosity function suggest that there will be between 50 and 100 new quasars with $z > 6.0$ across the $\sim 5000 \text{ deg}^2$ of the full DES area down to $Y_{\text{AB}} = 21.5$. The predictions also suggest that there

will be 3–10 quasars with $z > 6.5$ and $Y_{AB} < 21.5$ found in the complete survey footprint.

Estimates from the Willott et al. (2010) and McGreer et al. (2013) luminosity functions suggest that there are 5–10 quasars with $z < 6.5$ in the SVA1 area. Our selection method gives 43 other candidate objects and suggests four as higher priority than the others. This final selection step is biased towards bright objects, due to them having smaller errors than fainter candidates, and is not designed to find a complete sample. To find all the quasars in this area with a high purity would require full Bayesian analysis of the quasar population and the brown dwarfs. The exact number of quasars predicted in our survey is also sensitive to the choice of quasar template. Different predictions for the Ly α forest in these quasar template spectra can change the exact redshift range probed by our colour selection criteria. This then heavily influences the predicted number of objects.

6 CONCLUSIONS

We have presented the first search for high-redshift quasars in the DES using 291 deg² of optical imaging data from the DES SV observations. Our search algorithms are demonstrated to be effective in removing image artefacts and spurious sources such as cosmic rays and satellite trails that can populate the same regions of colour space as rare objects in the data. Based on the DES photometric data alone, we were able to reduce the number of candidates in this region to a size suitable for visual inspection. We also did not require confirmation photometric follow-up as has been the case in previous high-redshift ($z > 6$) quasar searches. A photometric error-weighted colour selection metric was introduced as a method of ranking candidates according to the probability of being high-redshift quasars. The highest ranked candidate, DESJ0454–4448 was spectroscopically confirmed to be a high redshift quasar at $z = 6.10$. Three more candidates were also identified as having colours consistent with high-redshift quasars and will be further investigated as part of the larger sample of high-redshift quasar candidates from the DES Year 1 observations.

DESJ0454–4448 is also detected at infrared wavelengths in the VISTA Hemisphere Survey and the WISE All-Sky Survey and its infrared colours are entirely consistent with those expected for high-redshift quasars. Using current estimates of the $z \sim 6$ quasar luminosity function, we have shown that the first $z \sim 6$ quasar is expected in the 291 deg² region used in this work, at a z -band magnitude of 20.2. The measured z -band magnitude of DESJ0454–4448 is 20.2, entirely consistent with these predictions.

We conclude that our search algorithms for high-redshift quasars are successful in isolating quasars at $z > 6$ from DES photometry alone. The analysis method presented here should be easily scalable to the full 5000 deg² area of DES and is therefore expected to result in substantial numbers of new high-redshift quasars in the Southern hemisphere over the next few years.

ACKNOWLEDGEMENTS

RGM, SLR and MB acknowledge the support of UK Science and Technology research Council (STFC).

We are grateful for the extraordinary contributions of our CTIO colleagues and the DES Camera, Commissioning and Science Verification teams in achieving the excellent instrument and telescope conditions that have made this work possible. The success of this project also relies critically on the expertise and dedication of the DES Data Management organization.

Funding for the DES Projects has been provided by the US Department of Energy, the US National Science Foundation, the Ministry of Science and Education of Spain, the Science and Technology Facilities Council of UK, the Higher Education Funding Council for England, the National Center for Supercomputing Applications at the University of Illinois at Urbana-Champaign, the Kavli Institute of Cosmological Physics at the University of Chicago, Financiadora de Estudos e Projetos, Fundação Carlos Chagas Filho de Amparo à Pesquisa do Estado do Rio de Janeiro, Conselho Nacional de Desenvolvimento Científico e Tecnológico and the Ministério da Ciência e Tecnologia, the Deutsche Forschungsgemeinschaft and the Collaborating Institutions in the DES.

The Collaborating Institutions are Argonne National Laboratories, the University of California at Santa Cruz, the University of Cambridge, Centro de Investigaciones Energeticas, Medioambientales y Tecnológicas-Madrid, the University of Chicago, University College London, the DES-Brazil Consortium, the Eidgenössische Technische Hochschule (ETH) Zurich, Fermi National Accelerator Laboratory, the University of Edinburgh, the University of Illinois at Urbana-Champaign, the Institut de Ciències de l'Espai (IEEC/CSIC), the Institut de Física d'Altes Energies, the Lawrence Berkeley National Laboratory, the Ludwig-Maximilians Universität and the associated Excellence Cluster Universe, the University of Michigan, the National Optical Astronomy Observatory, the University of Nottingham, The Ohio State University, the University of Pennsylvania, the University of Portsmouth, SLAC National Laboratory, Stanford University, the University of Sussex, and Texas A&M University.

This paper has gone through internal review by the DES collaboration.

The analysis presented here is based on observations obtained as part of the VISTA Hemisphere Survey, ESO Programme, 179.A-2010 (PI: McMahon).

ACR acknowledges financial support provided by the PAPDRJ CAPES/FAPERJ Fellowship.

REFERENCES

- Assef R. J. et al., 2010, *ApJ*, 713, 970
 Banerji M. et al., 2015, *MNRAS*, 446, 2523
 Becker G. D., Rauch M., Sargent W. L. W., 2007, *ApJ*, 662, 72
 Blain A. W. et al., 2013, *ApJ*, 778, 113
 Bolton J. S., Haehnelt M. G., 2007, *MNRAS*, 374, 493
 Carilli C. L. et al., 2010, *ApJ*, 714, 834
 Carnall A. C. et al., 2015, *MNRAS*, 451, L16
 Danforth C. W., Keeney B. A., Stocke J. T., Shull J. M., Yao Y., 2010, *ApJ*, 720, 976
 Desai S. et al., 2012, *ApJ*, 757, 83
 Fan X., White R. L., Davis M., Becker R. H., Strauss Z., 2000, *AJ*, 120, 1167
 Fan X. et al., 2001, *ApJ*, 122, 2833
 Fan X., Strauss M. A., Richards G. T., Hennawi J. F., Becker R. H., White R. L., Diamond-Stanic A. M., Donley J. L., 2006, *AJ*, 131, 1203
 Fan X. et al., 2006, *ApJ*, 132, 117
 Flaugher B. L., Abbott T. M. C., Angstadt R., Annis J., Antonik M. L., Bailey J., Ballester O., 2012, in McLean I. S., Ramsay S. K., Takami H., eds, *Proc. SPIE Conf. Ser. Vol. 8446, Ground-based and Airborne Instrumentation for Astronomy IV*. SPIE, Bellingham, p. 844611
 Gunn J. E., Peterson B. A., 1965, *ApJ*, 142, 1633
 Hook I. M., McMahon R. G., 1998, *MNRAS*, 294, L7
 Jarrett T. H. et al., 2011, *ApJ*, 735, 112
 Jiang L. et al., 2009, *AJ*, 138, 305
 Marshall J. L. et al., 2008, in McLean I. S., Casali M. M., eds, *Proc. SPIE Conf. Ser. Vol. 7014, Ground-based and Airborne Instrumentation for Astronomy II*. SPIE, Bellingham, p. 701454

- McGreer I. D. et al., 2013, *ApJ*, 768, 105
- McMahon R. G., Banerji M., Gonzalez E., Kogosov S. E., Bejar B. V. J., Lodiou N., Rebolo R., VHS Collaboration 2013, *The Messenger*, 154, 35
- Mohr J. J. et al., 2012, in Radziwill N. M., Chiozzi G., eds, *Proc. SPIE Conf. Ser. Vol. 8451, Software and Cyberinfrastructure for Astronomy II*. SPIE, Bellingham, p. 84510D
- Mortlock D. J. et al., 2011, *Nature*, 474, 616
- Mortlock D. J., Patel M., Warren S. J., Hewett P. C., Venemans B. P., McMahon R. G., Simpson C., 2012, *MNRAS*, 419, 390
- Planck Collaboration XIII, 2015, preprint ([arXiv:1502.01589](https://arxiv.org/abs/1502.01589))
- Richards G. T., Fan X., Newberg H. J., Strauss M. A., Vanden Berk D. E., Schneider D. P., Yanny B., 2002, *AJ*, 123, 2945
- Schmidt M., Green R. F., 1983, *ApJ*, 269, 352
- Stern D. et al., 2012, *ApJ*, 753, 30
- Storrie-Lombardi L. J., Irwin M. J., McMahon R. G., Hookook I. M., 2001, *MNRAS*, 322, 933
- Stoughton C. et al., 2002, *AJ*, 123, 485
- Swanson M. E. C., Tegmark M., Hamilton A. J. S., Hill J. C., 2008, *MNRAS*, 387, 1391
- The Dark Energy Survey Collaboration, 2005, preprint ([astro-ph/0510346](https://arxiv.org/abs/astro-ph/0510346))
- Venemans B. P. et al., 2013, *ApJ*, 779, 24
- Venemans B. P. et al., 2015, *ApJ*, 801, L11
- Véron-Cetty M.-P., Véron P., 2010, *A&A*, 518, A10
- Willott C. J. et al., 2010, *AJ*, 139, 906
- Wright E. L. et al., 2010, *ApJ*, 140, 1868
- Wu X.-B. et al., 2015, *Nature*, 518, 512

APPENDIX A: EXPLORATORY DATA ANALYSIS

Given below are some examples of the types of object removed during each step of the selection process.

A1 Flags

The DES flags were used as detailed in step one of Section 3. In Fig. A1 we show examples of objects that fail only the first part of our flag cuts. As can be seen most of these objects are junk rather than valid candidates. The central cutout shows an object that is undetected in that band which are exactly the objects that we want to keep in the g and r bands as they correspond to high-redshift quasar candidates. To ensure that candidates were not removed objects were only removed if they failed both of the flag cuts. The second cut was made in the weight flags and the combination of these removed the junk objects but kept the faint, undetected sources in.

The internal flags that are produced by *SEXTRACTOR* are as follows.

- (i) 1 – The object has neighbours, bright and close enough to significantly bias the MAG AUTO photometry, or bad pixels (more than 10 per cent of the integrated area affected).
- (ii) 2 – The object was originally blended with another one.

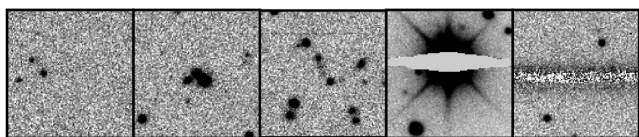


Figure A1. All of the objects shown here are flagged with a three in the DES flags. It can be seen that all of these objects have very different problems with them and that the first cutout shows an object that we would want to keep in if it looked like that in the g or r band. These cutouts are 30 arcsec by 30 arcsec and all taken from the z -band images. The flagging was found to be similar across all the bands and objects shown here have many analogies in the other bands.

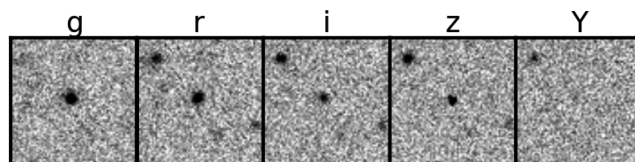


Figure A2. In these cutouts an object is shown with $g_{\text{psf}} = 23.16 \pm 0.03$ and $r_{\text{psf}} = 23.02 \pm 0.03$. The source is obviously detected in the g and r band despite having a magnitude below our limit.

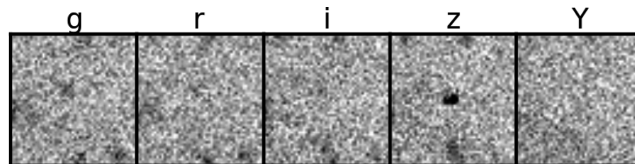


Figure A3. This object has no discernible flux in the g band but a catalogue entry of $g_{\text{psf}} = 24.88 \pm 0.15$ and has no detection in the r band. Despite appearing similar in both bands the object has been treated differently by the pipeline in each band; leading to a detection in one and not in the other. This demonstrates how the selection technique for dropouts has to take into account the multiple ways of treating objects at the detection threshold.

- (iii) 4 – At least one pixel of the object is saturated (or very close to).
- (iv) 8 – The object is truncated (too close to an image boundary).
- (v) 16 – Object's aperture data are incomplete or corrupted.
- (vi) 32 – Object's isophotal data are incomplete or corrupted.
- (vii) 64 – A memory overflow occurred during deblending.
- (viii) 128 – A memory overflow occurred during extraction.

This information was taken from the *SEXTRACTOR* documentation.

These flags are produced for each band and are included in the DES DM data base products.

A2 g - and r -band detections

In steps 5 and 6 a catalogue based method for removing objects that are detected in the bluer bands is used. First objects with a magnitude brighter than 23 were removed. It was found that this did not reliably remove all detected objects. Some objects were in a particularly deep part of the survey and still had a clean detection, shown in Fig. A2, despite being fainter than 23rd magnitude. To remove these an error cut was used, sources with $\sigma_{g/r} > 0.1$ were kept.

The cut of $\sigma_{g/r} > 0.1$ was used as it was empirically found from the data that this was a good balance between keeping a few faint objects and not throwing away objects that were falsely detected in g or r . Positive noise at the site of the object can cause *SEXTRACTOR* to register a magnitude for the object when there is not a clean detection. This is shown in the cutouts in Fig. A3.

As high-redshift quasars are unlikely to be detected in the g or r bands it is important that objects with a false detection in g or r are kept.

Another problem that was found was that some objects had a $g/r_{\text{psf}} = 99$ (which can mean a non-detection) but were actually very bright, saturated objects. An example of this is shown in Fig. A4.

The object in Fig. A4 has the same r -band magnitude as the object shown in Fig. A3. To distinguish between these two cases a rough version of forced photometry was used as described in step 9 of Section 3. As the difference in flux values for these two categories

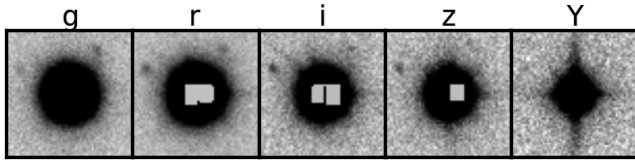


Figure A4. Here an object which has saturated in the *g* and *r* bands is shown. While it is obviously present in all the bands its PSF magnitudes are 99. This objects has $g_{\text{psf}} = 99.0 \pm 1.0$, $r_{\text{psf}} = 99.0 \pm 1.0$, $i_{\text{psf}} = 99.0 \pm 1.0$ and $z_{\text{psf}} = 14.7326 \pm 0.0001$.

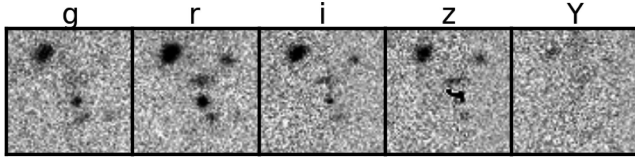


Figure A5. Cosmic ray hits in the *z* band create objects that pass the selection due to looking like extremely red *i* – *z* dropouts. These cutouts show the odd shape of the cosmic ray as well as demonstrating that they are not smoothed out by the PSF.

of object is very dramatic and the *r*-band magnitudes were not required a complicated method of accurate forced photometry was not needed.

A3 Cosmic ray removal

A cosmic ray hit in the *z* band can cause an object to pass the selection criteria as it looks like a very extreme *i* – *z* dropout. An example cosmic ray detection is shown in Fig. A5, this shows the irregular shape of the detection.

The first step in removing these objects, which made up most of our sample after step 7 in Section 3, was to require the objects to have a *Y*-band magnitude. As the *Y*-band data are shallower and more variable than the other bands no error cut was used. This left in objects that were false detections in the *Y* band (such as the object in Fig. A5 which has $Y_{\text{psf}} = 20.54 \pm 1.0$) and the candidate list was still swamped with cosmic rays. To remove these image based cosmic ray removal was used. This step worked off the differences between adjacent pixels as it was found that real objects had much shallower gradients between adjacent pixels than cosmic rays.

A4 SQL used

Here we present the SQL code used to query the DES data base. This code returns 838 rows from a data base with 40 129 963 unique sources as shown in steps 1–8b in Table 1.

```
SELECT
*
FROM
SVA1_COADD_GRIZY
WHERE
/* Flag criteria */
(FLAGS_G = 0 OR FLAGS_WEIGHT_G = 0 OR
FLAGS_G > 3) AND
(FLAGS_R = 0 OR FLAGS_WEIGHT_R = 0 OR
```

```
FLAGS_R > 3) AND
(FLAGS_I = 0 OR FLAGS_WEIGHT_I = 0 OR
FLAGS_I > 3) AND
(FLAGS_Z = 0 OR FLAGS_WEIGHT_Z = 0 OR
FLAGS_Z > 3) AND
(FLAGS_Y = 0 OR FLAGS_WEIGHT_Y = 0 OR
FLAGS_Y > 3) AND

/* Z band limits */
MAG_PSF_Z <= 21.5 AND MAGERR_PSF_Z < 0.1

AND

/* Morphological criterion */
MAG_PSF_Z - MAG_MODEL_Z < 0.145 AND

/* I-Z colour criterion */
MAG_PSF_I - MAG_PSF_Z > 1.694 AND

/* G and R dropout criteria */
MAG_PSF_G > 23 AND MAG_PSF_R > 23 AND
MAGERR_PSF_G > 0.1 AND
MAGERR_PSF_R > 0.1 AND

/* Z-Y colour criterion */
MAG_PSF_Z - MAG_PSF_Y < 0.5 AND

/* Y band detection criterion */
MAG_PSF_Y <> 99 AND
MAG_PSF_Y < 23
```

¹*Institute of Astronomy, University of Cambridge, Madingley Road, Cambridge CB3 0HA, UK*

²*Kavli Institute for Cosmology, University of Cambridge, Madingley Road, Cambridge CB3 0HA, UK*

³*Department of Physics and Astronomy, University College London, Gower Street, London WC1E 6BT, UK*

⁴*Space Telescope Science Institute, 3700 San Martin Dr, Baltimore, MD 21218, USA*

⁵*Center for Cosmology and Astro-Particle Physics, The Ohio State University, Columbus, OH 43210, USA*

⁶*Department of Astronomy, The Ohio State University, Columbus, OH 43210, USA*

⁷*Observatories of the Carnegie Institution for Science, 813 Santa Barbara Street, Pasadena, CA 91101, USA*

⁸*Cerro Tololo Inter-American Observatory, National Optical Astronomy Observatory, Casilla 603, La Serena, Chile*

⁹*Fermi National Accelerator Laboratory, PO Box 500, Batavia, IL 60510, USA*

¹⁰*Institut d'Astrophysique de Paris, Univ. Pierre et Marie Curie and CNRS UMR7095, F-75014 Paris, France*

¹¹*SLAC National Accelerator Laboratory, Menlo Park, CA 94025, USA*

¹²*Observatório Nacional, Rua Gal. José Cristino 77, Rio de Janeiro, RJ 20921-400, Brazil*

¹³*Laboratório Interinstitucional de e-Astronomia - LIneA, Rua Gal. José Cristino 77, Rio de Janeiro, RJ 20921-400, Brazil*

¹⁴*Institute of Cosmology and Gravitation, University of Portsmouth, Portsmouth PO1 3FX, UK*

¹⁵*George P. and Cynthia Woods Mitchell Institute for Fundamental Physics and Astronomy, and Department of Physics and Astronomy, Texas A&M University, College Station, TX 77843, USA*

¹⁶*Department of Physics, Ludwig-Maximilians-Universität, Scheinerstr. 1, D-81679 München, Germany*

¹⁷Kavli Institute for Particle Astrophysics & Cosmology, PO Box 2450, Stanford University, Stanford, CA 94305, USA

¹⁸Department of Physics, University of Michigan, Ann Arbor, MI 48109, USA

¹⁹Institut de Ciències de l'Espai, IEEC-CSIC, Campus UAB, Facultat de Ciències, Torre C5 par-2, E-08193 Bellaterra, Barcelona, Spain

²⁰University Observatory Munich, Scheinerstrasse 1, D-81679 Munich, Germany

²¹Australian Astronomical Observatory, North Ryde, NSW 2113, Australia

²²ICRA, Centro Brasileiro de Pesquisas Físicas, Rua Dr. Xavier Sigaud 150, CEP 22290-180 Rio de Janeiro, RJ, Brazil

²³Institut de Física d'Altes Energies, Universitat Autònoma de Barcelona, E-08193 Bellaterra, Barcelona, Spain

²⁴Brookhaven National Laboratory, Bldg 510, Upton, NY 11973, USA

²⁵Department of Physics and Astronomy, University of Pennsylvania, Philadelphia, PA 19104, USA

²⁶Centro de Investigaciones Energéticas, Medioambientales y Tecnológicas (CIEMAT), E-28040 Madrid, Spain

²⁷Instituto de Física, UFRGS, Caixa Postal 15051, Porto Alegre, RS - 91501-970, Brazil

²⁸Department of Physics, The Ohio State University, Columbus, OH 43210, USA

²⁹National Centre for Supercomputing Applications, 1205 West Clark St., Urbana, IL 61801, USA

³⁰SEPnet, South East Physics Network (www.sepnet.ac.uk)

³¹Department of Physics, Stanford University, 382 Via Pueblo Mall, Stanford, CA 94305, USA

This paper has been typeset from a $\text{\TeX}/\text{\LaTeX}$ file prepared by the author.